PHYSICS

Direct generation of spatially entangled qudits using quantum nonlinear optical holography

Ofir Yesharim[1]†, Shaul Pearl[1,2]†, Joshua Foley-Comer[1], Irit Juwiler[3], Ady Arie[1]*

Nonlinear holography shapes the amplitude and phase of generated new harmonics using nonlinear processes. Classical nonlinear holography influenced many fields in optics, from information storage, demultiplexing of spatial information, and all-optical control of accelerating beams. Here, we extend the concept of nonlinear holography to the quantum regime. We directly shape the spatial quantum correlations of entangled photon pairs in two-dimensional patterned nonlinear photonic crystals using spontaneous parametric down conversion, without any pump shaping. The generated signal-idler pair obeys a parity conservation law that is governed by the nonlinear crystal. Furthermore, the quantum states exhibit quantum correlations and violate the Clauser-Horne-Shimony-Holt inequality, thus enabling entanglement-based quantum key distribution. Our demonstration paves the way for controllable on-chip quantum optics schemes using the high-dimensional spatial degree of freedom.

INTRODUCTION

Holography is a method of storing the amplitude and phase information of a wave packet and reconstructing it by illuminating the hologram with a reference wave. Holography was invented by Dennis Gabor back in 1948 (*1*) for electron microscopy applications. Since then, it has been extensively used for many types of waves. Perhaps the most well-known use of holograms is in the field of light optics (*2*), where the ability to shape the wavefront of light beams has found numerous applications including microscopy (*3*), particle trapping (*4*), optical communication (*5*), anti-counterfeiting (*6*), and many more.

Whereas the standard hologram reconstructs the desired beam at the same wavelength as that of the reference wave, many cases require shaping the generated beam at a different wavelength. One possible solution is to perform nonlinear conversion (*7*), followed by beam shaping using an additional hologram (Fig. 1A). However, in the past decade, a new type of hologram has emerged, where a reference wave illuminates a nonlinear crystal, and the spatially reconstructed beam emerges at a new wavelength, for example, at the second harmonic of the reference wave (Fig. 1B) (*8*–*13*). This led to a plethora of optical functionalities such as generating and controlling beams with accelerated trajectory (*14*) or with orbital angular momentum (*15*) as well as multiplexing of spatial modes of light using cascaded designs (*16*).

For nonlinear holography to occur, the interacting waves must satisfy either complete phase matching or at least quasi–phase matching (QPM) (*7*). QPM is realized by periodic modulation of the nonlinear coefficient along the propagation direction. Owing to this periodic pattern of the nonlinearity, the structured nonlinear crystals are often called nonlinear photonic crystals (NPCs) (*9*, *17*, *18*). Nonlinear holography is now achievable by modulating the nonlinear coefficient of the crystal using coding schemes that are similar to those that were developed for traditional holography (*19*, *20*) while maintaining the QPM conditions.

In addition to stimulated nonlinear processes such as second-harmonic generation or sum frequency generation, spontaneous nonlinear optical processes are at the heart of many quantum information schemes. Notably, the process of spontaneous parametric downconversion (SPDC) is the source for many quantum optics experiments (*21*). During SPDC, a pump photon spontaneously splits to pairs of correlated photons, named signal and idler. These correlations can manifest themselves in many degrees of freedom such as polarization (*21*), frequency (*22*) - where shaped crystals is successfully used for shaping the spectral degree of freedom (*23*, *24*), and spatial mode patterns (*25*). In light-based quantum information, and specifically in high-dimensional quantum information protocols (*25*, *26*), the spatial degree of freedom spans a multidimensional Hilbert space. This provides a larger alphabet for encoding information on a single photon, with respect to the common two-dimensional (2D) Hilbert space. Furthermore, the higher dimensionality also increases the error threshold in quantum key distribution applications (*27*, *28*). Shaping these high-dimensional quantum states was first performed two decades ago by pump beam shaping–based SPDC (*29*), followed by signal/idler shaping (*30*). These external shaping methods have since been the main driving force behind high-dimensional quantum state engineering. To this day, while theoretically proposed by a number of works (*31*–*34*), the crystal degree of freedom was not demonstrated experimentally for spatial encoding of quantum light.

Driven by the recent interest in high-dimensional entanglement, in this work, we use nonlinear holograms to shape the spatial quantum correlations of entangled photon pairs generated in a type 2 SPDC process without any pump shaping (Fig. 1C). By borrowing concepts from computer-generated holograms, we imprint Hermite-Gauss (HG) patterns in an NPC. This enables us to engineer spatially entangled qubits and qudits that can be used in quantum information protocols. The HG basis was chosen because the spatial modes span a multidimensional Hilbert space, they preserve their shape while propagating in free space (except for expansion owing to diffraction), and they are orthogonal to

[1]School of Electrical Engineering, Fleischman Faculty of Engineering, Tel Aviv University, Tel Aviv, Israel. [2]Applied Physics Division, Soreq NRC, Yavne, Israel. [3]Department of Electrical and Electronics Engineering, Shamoon College of Engineering, Ashdod, Israel.
*Corresponding author. Email: ady@tauex.tau.ac.il
†These authors contributed equally to this work.

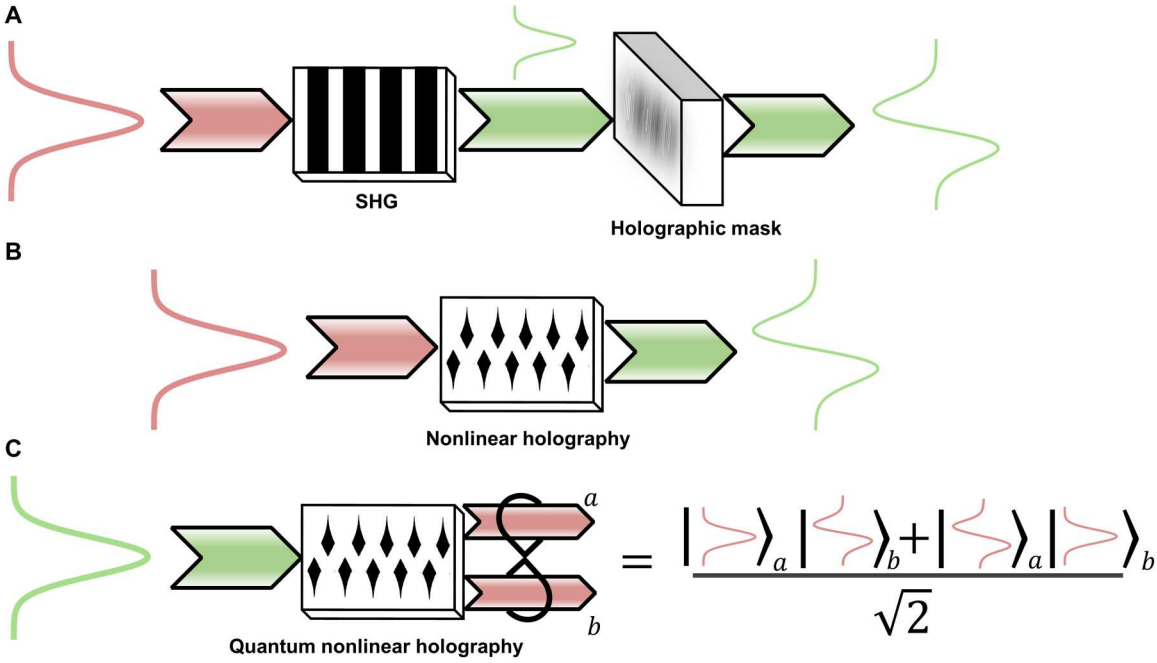

Fig. 1. Conceptual illustration of classical and quantum nonlinear holography. (**A**) In classical holography, the fundamental pump beam enters a nonlinear crystal and generates a Gaussian-shaped second harmonic. The second-harmonic beam is then shaped using a linear holographic mask. SHG, second-harmonic generation. (**B**) In classical nonlinear holography, the second-harmonic beam is spatially shaped entirely inside the nonlinear crystal by the modulated nonlinearity. (**C**) In quantum nonlinear holography, the quantum correlations between different spatial transverse modes of downconverted photons are shaped using the modulated nonlinearity.

each other, but the same method can be extended in the future to other sets of spatial modes, such as the Laguerre-Gauss modes. Our method miniaturizes the quantum shaping process to the bare minimum; only a laser, an NPC, and a polarizing beam splitter (PBS) are required, saving the need for additional optical elements—a crucial step for integrated quantum optics or miniaturized bulk quantum optics schemes. For the NPCs, we use $KTiOPO_4$ (KTP) crystals, a current workhorse of SPDC-based quantum optics schemes because of its high nonlinearity, wide transparency range, and optical quality (*21*). KTP crystals were considered difficult for 2D electric field poling because of their anisotropic nature (*35*); however, here, we have found conditions that enable the realization of the required pattern by electric field poling.

RESULTS

Because HG functions form a complete basis of orthogonal transverse modes, we can decompose the two-photon state generated by SPDC using HG ket vectors in transverse momentum space q of the signal and idler waves (*36*, *37*)

$$|\Psi\rangle = C_0|0\rangle + \sum_{jk}\sum_{ut} C_{jkut}|\mathrm{HG}_{jk}(\vec{q},\sigma)\rangle_i|\mathrm{HG}_{ut}(\vec{q},\sigma)\rangle_s \quad (1)$$

where j,u (k,t) are the "X"("Y") mode numbers of the signal and idler, $|0\rangle$ is the vacuum state, C_{jkut} values are the coefficients of the generated biphoton state, and $\vec{q}$ is the transverse momenta of the signal and idler. Here, we assume that both the signal and the idler have the same waist radius σ. The coefficients C_{jkut} depend on the nonlinear coupling (see the Supplementary Materials), thus enabling the control of the generated state. The spatial 2D engineering of $\chi^{(2)}$ in ferroelectric crystals is possible, for example, through electric field poling where the nonlinearity changes sign. Specifically, we used Lee's (*19*) method of binary computer holograms [modified for on-axis nonlinear beam shaping (*38*)] to imprint the desired function onto the NPC. Consider a nonlinear crystal with the following modulated nonlinearity

$$\chi^{(2)}(\vec{r}) = \chi^{(2)}\mathrm{sign}\{\cos[2\pi\Delta k z + \phi(z,x)] - \cos[\pi q(z,x)]\} \quad (2)$$

where $q(z,x) = \sin^{-1}\frac{A(z,x)}{\pi}$, $A(z,x) \in [0,1]$ is the amplitude of the desired function, $\phi(z,x)$ is its phase, $\chi^{(2)}$ is the nonlinear coefficient, and $\Delta k = k_p - k_S - k_i$ is the phase mismatch for a colinear interaction.

Assuming that only the first-order interaction is phase-matched and that all other orders are far from phase matching and can be neglected (see the Supplementary Materials for details), we get the following expression for the nonlinear coupling

$$\chi^{(2)}(\vec{r})\psi_p(\vec{r}) \propto A(z,x)e^{i\phi(z,x)}e^{\frac{i2\pi}{\Lambda}z}e^{-\frac{x^2}{W_p^2(z)}} \quad (3)$$

where we assumed a Gaussian pump input, ψ_p, with waist size W_p, and Λ is the periodicity of the nonlinear crystal. Thus, the quantum state can be engineered using a shaped pump, structured crystal, or both.

Furthermore, it was shown in (*39*) that the following parity conservation for HG modes is satisfied between the generated signal and idler in the X axis and the pump beam

$$\mathrm{Parity}(j+u) = \mathrm{Parity}(n) \quad (4)$$

where n is the illuminating pump mode number in the X axis. In this work, we pump the crystal with a Gaussian beam (hence,

$n = 0$), but because the crystal is structured, the pump index n is replaced by n_c, the nonlinear crystal mode number. This means that if the crystal index n_c is odd (even), the sum of the indices of the idler and signal beams along the X axis must also be odd (even). As an example, for an HG_{10} mode crystal, $n_c = 1$; hence, the two possible signal-idler pairs are $|HG_{10}\rangle_i|HG_{00}\rangle_s$ and $|HG_{00}\rangle_i|HG_{10}\rangle_s$. In general, there are additional signal-idler pairs that can satisfy the parity conservation rule, but we can eliminate them and maintain only the two aforementioned pairs by proper selection of the crystal pattern and pump width. Therefore, the generated signal and idler mode distribution depends on the spatial mode number, the physical size of the nonlinear crystal pattern, and the illuminating beam (see the Supplementary Materials for detailed derivation).

As noted above, 2D electric field poling of KTP is considered very difficult, owing to its high anisotropy. Here, we overcome this difficulty by working under conditions where the quasi–phase-matched poling period is very large [~450 μm, about two orders of magnitude larger with respect to periods that are typically used in KTP for SPDC in the visible and near infrared (*40*)] and by approximating the "rounded" shapes of the poling pattern with a set of rectangular patterns (see Materials and Methods regarding crystal fabrication). A comparison between the designed pattern and the fabricated pattern is shown in Fig. 2 (B and C).

To characterize the nonlinear holograms, we first used a second-harmonic generation process (see Materials and Methods). The nonlinear holographic patterns will generate an on-axis HG_{10} or HG_{20} beam at the second harmonic, depending on the nonlinear hologram. Figure 3 shows the near- and far-field patterns of these beams.

Next, we used the experimental setup depicted in Fig. 2A to measure the quantum correlations between different spatial mode profiles of the signal and idler photons generated using quantum nonlinear holography. The experimental setup (Fig. 2) consists of state generation and measurement (see Materials and Methods for a detailed description). The quantum light source is based on a degenerate type 2 SPDC process that generates two orthogonally polarized (H, V) 1064.5-nm photons. The photon pairs were split by a PBS and relay-imaged onto two halves of a rectangular phase–only spatial light modulator (SLM) (Holoeye Pluto). The SLM spatially matches between the shapes of the impinging photons and the shapes of the two single-mode fibers that coupled the light to the detectors. Thus, it acts as a measurement tool for specific transverse spatial modes (*25*, *36*). By realizing a patterned blazed grating on the

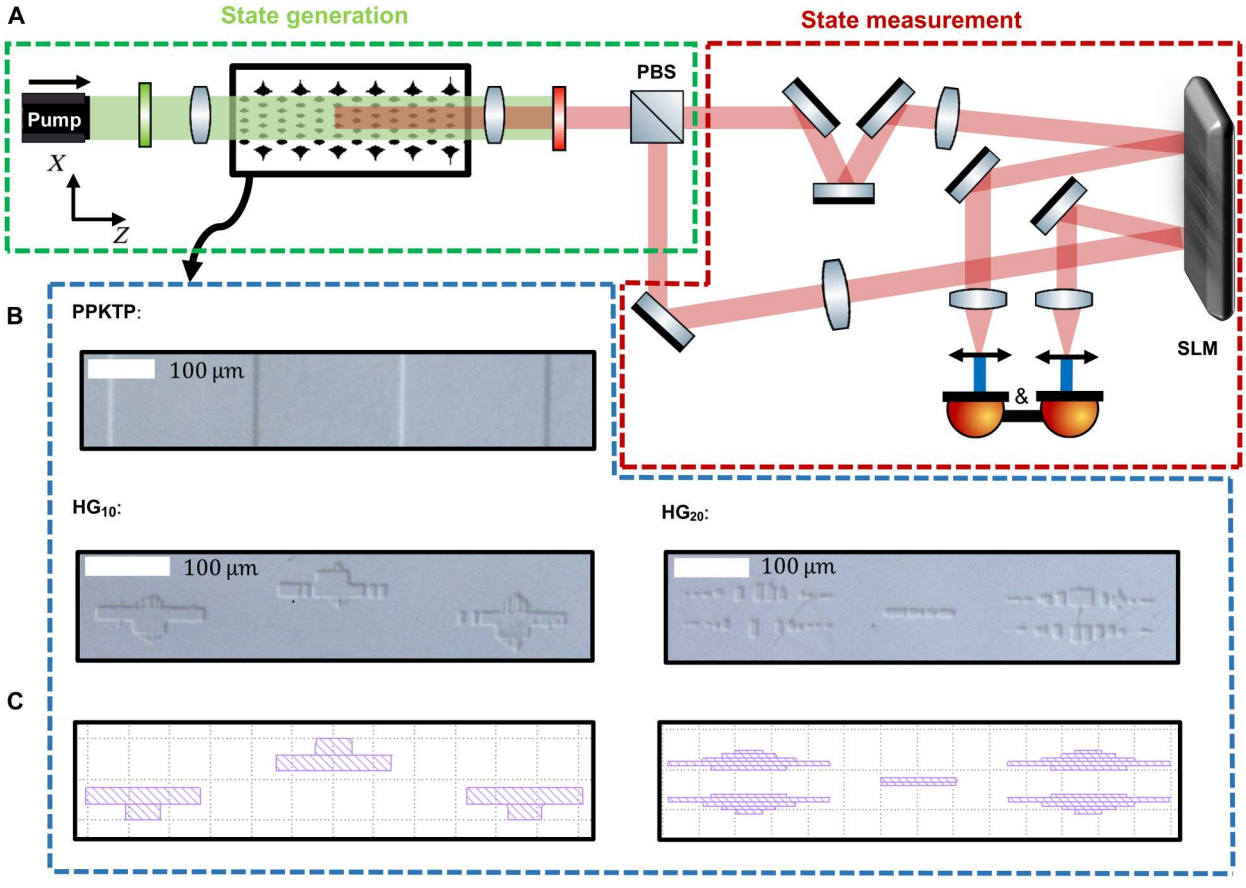

Fig. 2. Experimental setup. (**A**) A continuous wave (CW) 532.25-nm pump is focused to the patterned KTP crystal. The pump beam is filtered, and the photon pairs are split using a PBS. The H- and V-polarized photons are then sent to two halves of an SLM, after rotation of the V-polarized photon to an H-polarized photon (not shown in the figure). Photons from the first diffraction order of the SLM were coupled to two single-mode fibers followed by two "single-quantum" SNSPDs for coincidence counting, with a coincidence window of 2.5 ns. (**B**) Microscopic pictures of the top surface of the fabricated crystals after selective etching that reveals the nonlinear modulation pattern in the $HG_{10\backslash 20}$ case and in a regular periodically poled KTP (PPKTP) case. (**C**) Original design of the nonlinear crystal. Left, HG_{10}; right, HG_{20}.

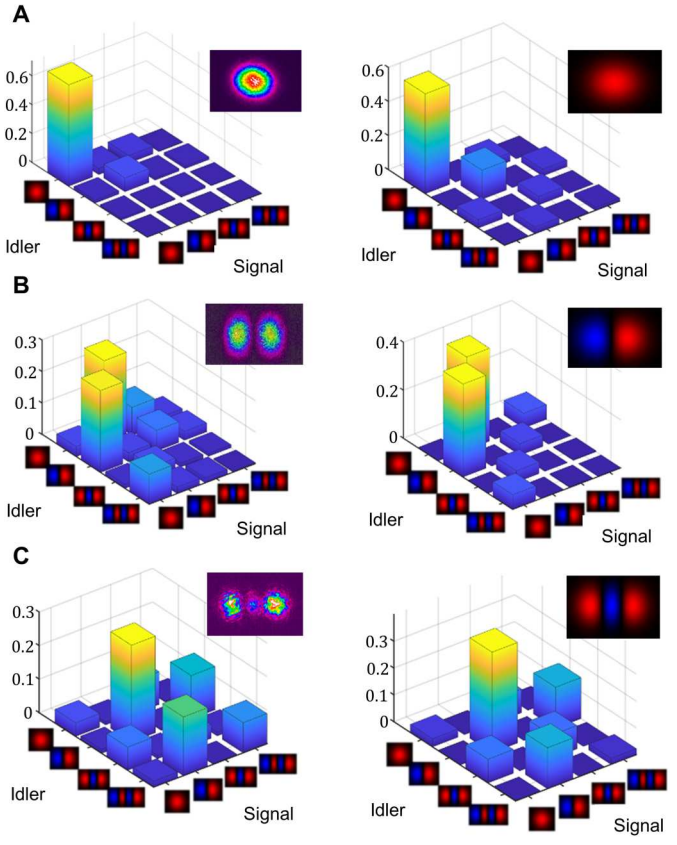

Fig. 3. Classical nonlinear holography and normalized coincidence detection rate for quantum nonlinear holography. (**A** to **C**) Normalized coincidence counts that correspond to the generated quantum state coefficients in the HG basis (*X* axis) for different nonlinear holograms. Left: Experimental measurements. Right: Corresponding simulations. Insets: Second-harmonic generation from the nonlinear holograms (left) and theoretical amplitudes of HG beam (right). (A) When the crystal is a regular PPKTP, only a single coefficient is nonzero. (B) For an HG_{10}-shaped crystal, the generated state is a Bell state of the HG_{00} and HG_{10} modes. (C) For the short HG_{20}-shaped crystal, the state coefficients are no longer concentrated and exhibit even parity of the sum of the horizontal mode indices.

SLM (*41*), we manipulate both the amplitude and phase of the photons incident on the SLM. By changing the SLM's patterns and measuring the coincidence rate, we can map the coefficients of the decomposed biphoton state and verify the corresponding generated biphoton quantum state (Fig. 3).

Different nonlinear holograms were used to shape the quantum correlations between the down converted photons (all kept at a temperature of 33°C). Because we shape the *X* axis of the crystal, we characterized the quantum states using the *X*-axis coefficients C_{ju}, assuming that the modes are Gaussian in the orthogonal *Y* axis (k, $t = 0$). First, we used a 1-cm HG_{10}-shaped nonlinear hologram (Fig. 2B) and measured the corresponding coincidence rate (Fig. 3B). Besides odd parity with respect to the sum of the generated signal and idler mode number, the highest coincidence counts are obtained for two cases: when either the signal is an HG_{10} beam and the idler is an HG_{00} beam or vice versa. This forms a good approximation to the Bell state: $|\Psi\rangle \approx (|\mathrm{HG}_{00}, \mathrm{HG}_{10}\rangle + e^{i\phi}|\mathrm{HG}_{10}, \mathrm{HG}_{00}\rangle)/\sqrt{2}$. The generated state is unique in terms of its brightness because minimal postselection is needed (*36*). This is because we operate in the regime where the state is mainly entangled between the HG_{00} and HG_{10} modes (see derivation in the Supplementary Materials). For the HG_{10} hologram, the detected coincidence rate was 2700 coincidence counts/s or ~0.031 kHz/mW. Considering the transmission from the SLM and the optical elements (15% transmission), the superconducting nanowire single-photon detector (SNSPD) detection efficiency (~60% at 1064 nm), and the interference filters near the detectors (90% transmission), the generated coincidence rate is estimated to be 411,000 coincidence counts/s or 4.72 kHz/mW; hence, it is comparable to pump-based entangled states or polarization-entangled sources (*36*).

Next, we used a 0.65-cm-long HG_{20} nonlinear hologram as our quantum light source (Fig. 2B). In contrast to previous measurements, the measured coincidence rates (Fig. 3C) are less concentrated and spread over more combinations of signal/idler modes. In addition, even parity condition is well satisfied; specifically, the mode pair of highest coincidence is $|\mathrm{HG}_{10}\rangle_i|\mathrm{HG}_{10}\rangle_s$ where the sum of the signal and idler mode indices (1 + 1) has the same even parity as that of the crystal index (2). Moreover, other pairs of substantial coincidence ,e.g., $|\mathrm{HG}_{20}\rangle_i|\mathrm{HG}_{00}\rangle_s$, $|\mathrm{HG}_{00}\rangle_i|\mathrm{HG}_{20}\rangle_s$, $|\mathrm{HG}_{30}\rangle_i|\mathrm{HG}_{10}\rangle_s$, and $|\mathrm{HG}_{10}\rangle_i|\mathrm{HG}_{30}\rangle_s$, also satisfy the even parity condition. Furthermore, the coincidence rate when the sum of the generated signal and idler mode number is odd is near zero. We note that the parity condition of the signal-idler pairs occurs because the nonlinear hologram of the crystal is based on a single HG function. We can design a crystal that is based on the superposition of several HG functions, which will lift the parity constraint. A design example is given in the Supplementary Materials. Last, for comparison, we used a regular periodically poled KTP (PPKTP) and measured the coincidence rate between different transverse mode profiles of the signal and idler (Fig. 3B). The coincidence rate contains a highly visible single peak at $|C_{00}|$, with relatively small rates at other coefficients. A single visible peak is generated because we operated near the single spatial mode regime (see the Supplementary Materials).

To validate our experimental results, we used an SPDC numerical simulation tool, which is based on Heisenberg equations of motions for the signal and idler field operators that evolve under the SPDC Hamiltonian. The simulation tool is nonperturbative and accounts for diffraction. It assumes the undepleted pump approximation and paraxial propagation dynamics (*31*, *42*). For the HG_{10} nonlinear hologram, both the measured and simulated coefficients form a maximally entangled Bell state. Besides the coefficients C_{10} and C_{01}, other measured coefficients are relatively small and are attributed to the nonideality of the nonlinear hologram (these coefficients vanish in the simulation) and optical aberrations. For the HG_{20} nonlinear hologram, we find very good agreement between simulation and experiment. We attribute the improved agreement between simulation and experiment for the HG_{20} crystal to the fact that the crystal design was closer to the ideal structure, with respect to the HG_{10} case. Overall, we find in both cases good agreement between experiments and numerical simulation, although the poled structures are not ideal, making quantum nonlinear holography robust to imperfections.

To further characterize the generated quantum state, we performed a Bell-type inequality experiment (Fig. 4A), by projecting the generated state on different points on the Bloch sphere,

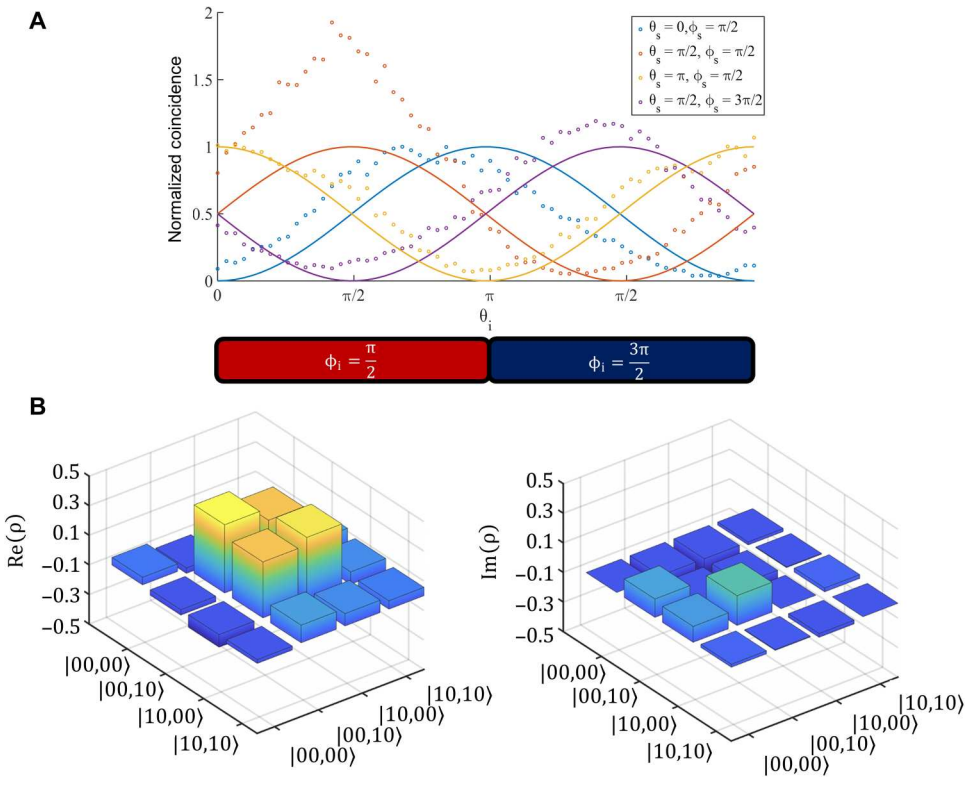

Fig. 4. Characterization of the spatial Bell state generated by an HG_{10}-shaped crystal. (**A**) A CHSH-type experiment. Each curve represents the projection of the signal photon on one of four points on the Bloch sphere characterized by $|\psi_s\rangle$. For each curve, the idler photon is continuously projected on different points on the Bloch sphere, with the horizontal axes representing the specific polar and azimuthal angles. Solid lines represent theoretical predictions. (**B**) Real (left) and imaginary (right) parts of the estimated density matrix.

characterized by (*36*, *43*): $|\psi_{i,s}\rangle = \cos(\theta_{i,s}/2)|HG_{00}\rangle + e^{i\phi_{i,s}} \sin(\theta_{i,s}/2)|HG_{10}\rangle$,where $\theta_{i,s}$ and $\phi_{i,s}$ are the polar and azimuthal angles of the 2D Bloch sphere for the idler and signal photons. We calculated the Clauser-Horne-Shimony-Holt (CHSH) S parameter and violated the CHSH inequality with $S = 2.379 \pm 0.118$. Hence, the system exhibits quantum correlations between the downconverted photons that cannot be explained classically. The increase in coincidence toward $\theta_{i,s} = \frac{\pi}{2}, \phi_{i,s} = \frac{\pi}{2}$ is due to the misalignment of the pump beam with respect to the nonlinear hologram (due to its high aspect ratio), creating a phase-matched noncolinear interaction that couples to the single-mode fiber in these angles. Furthermore, we performed experimental quantum state tomography (Fig. 4B) (*44*, *45*). The density matrix reconstruction was performed in a 2D space of the states $|HG_{00}\rangle$ and $|HG_{10}\rangle$ (see Materials and Methods). We calculated the fidelity $\mathcal{F} = 0.89$ of the generated state using an estimated density matrix, $\rho_{estimated}$, with respect to the ideal Bell state $|\Psi\rangle$ density matrix.

The generated state can be used as a source for quantum key distribution protocols based on entanglement, for example, the Ekert 91′ protocol (*46*, *47*). In this scheme, Alice and Bob receive the generated signal and idler photons, respectively. Then, through a series of random measurements and communication over a classical channel, they can securely share a secret key between them. When an eavesdropper, Eve, tries to interfere, the measured signal and idler photons will no longer break the CHSH inequality. This constitutes an error threshold for the channel security that Alice and Bob can use to detect attacks. Analogously, the quantum bit error rate (QBER), which is defined as the ratio of wrong bits to the total amount of detected bits, is a different measure for security criteria. For individual and coherent attacks by Eve, the quantum channel is secure for QBER < 15% and QBER < 11%, respectively (*47*). The QBER of our source is below these two thresholds: ~4.8% for $\theta_s = 0, \phi_s = \frac{\pi}{2}$ and 8.9% for $\theta_s = \frac{\pi}{2}, \phi_s = \frac{\pi}{2}$ for the Bell curves in Fig. 4A; hence, it is promising for practical implementations of quantum key distribution protocols (*48*).

DISCUSSION

To summarize, we introduced the concept of nonlinear holography to the quantum domain. We generated different spatially entangled states using nonlinear holography by shaping the nonlinearity of KTP crystals. The generated states exhibit high-fidelity quantum correlations and violate the CHSH inequality. Furthermore, the entanglement mode distribution changes between different crystal designs. There is no need to shape the pump, signal, or idler in the process, and the Gaussian pump remains Gaussian even after the nonlinear hologram, deeming it available for additional, different, state generation. The on-axis scheme allows for high-efficiency SPDC that does not require high pump intensities, allowing the generation of quantum states with a standard continuous wave (CW) laser. In addition, using a 2D modulated PPKTP allowed us to avoid photorefractive effects that may hinder the use of such devices in real-life scenarios (*49*, *50*).

From a fundamental point of view, in previous works on classical nonlinear holography, the nonlinear processes were stimulated, and the goal was to generate one shaped beam (e.g., in the second harmonic). Here, the process is spontaneous (hence fundamentally different); the generated signal and idler photons build up from the vacuum noise, and there are numerous possible pairs that can be generated. The quantum nonlinear hologram is therefore designed to select one or few specific signal-idler pairs while suppressing all other unwanted pairs. Moreover, the goal is to engineer not only the shape of the two generated beams but also their quantum correlations in a single optical element.

We believe that quantum nonlinear holography will be a key enabler in the field of high-dimensional entanglement based on spatial modes of light. It enables a compact and efficient generation of quantum light, a desirable property for satellite-based quantum networks (*21*, *51*). Moreover, by integrating patterned quasi–phase-matched structures with optical waveguides (*52*), few-mode optical waveguide entanglement can be fully engineered on-chip, without the need for free space beam manipulation (*53*, *54*). The binary modulation of the nonlinearity can be shaped in an arbitrary manner, in contrast to pump beams that must satisfy the Helmholtz equation. This enables the design of structures with a modulation pattern that varies along the propagation axis, for example, in a segmented manner, as well as cascaded patterns having different poling periods, facilitating all-optical control over the generated states (*8*, *16*, *31*, *33*). These segments may use various degrees of freedom: (i) Different phases between each segment will enable coherent destructive or constructive interference between states generated in a consecutive manner. (ii) Different waists in each segment can control each segment's mode distribution. (iii) Different transverse shapes govern parity and limit the allowed modes. Therefore, it would provide large flexibility in generating general quantum states in a compact manner, overcoming, to some extent, mode distribution constraints that are inherent in the creation of spatial mode entanglement. These are genuine quantum nonlinear holography features that cannot be reproduced using conventional shaping of the interacting waves. The method of approximating the NPC structure using a set of rectangles presented in our work may benefit the advent of 3D NPCs (*13*, *55*, *56*) and nonlinear metasurfaces (*57*). These structures will further increase the versatility of quantum nonlinear holography, allowing convenient shaping in both transverse axes, and giving full control over the nonlinear Ewald sphere (*16*). Last, whereas here we focused on generating light in a discrete set of spatial modes, the concept of quantum nonlinear holography can be readily extended to the regime of continuous variables, thereby simplifying complex optical setups with minimal change (*58*).

MATERIALS AND METHODS

Crystal fabrication

As explained in the results section, to cope with the anisotropy of KTP crystals, we approximated the crystal shapes that are based on binary computer-generated holography (*19*) using rectangular shapes. Figure 5 shows the difference between the ideal and approximated shapes. The rectangular shapes capture the main amplitude and phase features of the imprinted functions.

Second-harmonic generation characterization

For the second-harmonic generation process depicted in the insets of Fig. 3, we used a pump beam at the fundamental frequency (1064.5-nm Nd:YAG pulsed laser source) with 4.4-ns pulses at an 80-kHz repetition rate, working with a peak power of 0.82 W. The pump beam was focused to a waist radius of ~40 μm at the middle of the nonlinear crystal. The output was imaged using a 4f system with ×1.7 magnification.

Experimental setup

The pump is a 100-mW linearly polarized CW 532.25-nm laser with ~300 m of coherence length (Alphalas Monopower), which was focused to a ~40-μm waist radius inside the NPC. To eliminate the residual 1064.5-nm light, the pump beam was filtered by band-pass colored glass plates with ~90% total transmission at 532 nm and ~8 to 10 attenuation at 1064 nm. The measured pump power after the band-pass filter and a harmonic separator mirror was 87 mW. The photon pairs were split by a PBS and relay-imaged onto two halves of a rectangular phase–only SLM (Holoeye Pluto). To maximize the SLM efficiency, the V-polarized photon was rotated by a half–wave plate to be H-polarized. To eliminate radiation from the pump and stray light to reach the detectors, 1064-nm band-pass interference filters are placed after the SLM (shown after the NPC in Fig. 2). Emerging from the SLM after phase manipulations, photons from the first diffraction orders of the SLM are imaged to the entrance facets of the two fiber-coupled SNSPDs. The total optical paths of the photon pairs from the PBS to the fibers were set to be equal up to ~5 mm. The fibers are single mode and polarization maintaining for 1064 nm (PM980-XP). The detectors' efficiency is 68% (Single Quantum Eos), and the tagging system (Swabian Time Tagger 20) counts coincidence events on the two different arms occurring within less than 2.5 ns.

Quantum state tomography

The tomographic data were generated by projecting each of the signal and idler onto a subspace having different combinations of the spatial modes HG_{00} and HG_{01} with a relative phase of $\varphi = \left\{0, \frac{\pi}{2}, \pi, \frac{3\pi}{2}\right\}$ between them and measuring coincidence (*44*). Each combination is an eigenvector of the Pauli matrices for HG_{00} and HG_{01}.The measurement data can then be transformed into the density matrix using

$$\rho_{\text{experiment}} = \frac{1}{4}\sum_{m,n=0}^{3} \rho_{mn}\sigma_m \otimes \sigma_n \tag{M1}$$

where $\sigma_{m,n}$ values are the Pauli matrices whose eigenvectors correspond to different spatial combinations, and ρ_{mn} values are their expectation values. The expectation values, ρ_{mn}, were calculated from the tomographic data, with the help of the eigenvalues and eigenvectors corresponding to Pauli matrices σ_m and σ_n.

To ensure a physical density matrix—Hermitian with unit trace and non-negative eigenvalues—a maximum likelihood estimation was performed on the experimentally extracted density matrix against the target density matrix, $|\Psi\rangle$. The maximum likelihood estimation method (*45*) is based on optimizing the density matrix $\rho_{\text{est}} = TT^{\dagger}$, where T is a lower-triangular complex matrix, with regard to the tomography data. This translates into optimizing the real and imaginary variables t_i that constitute matrix T such that the expectation values of ρ_{est} in the tomographic measurement bases have

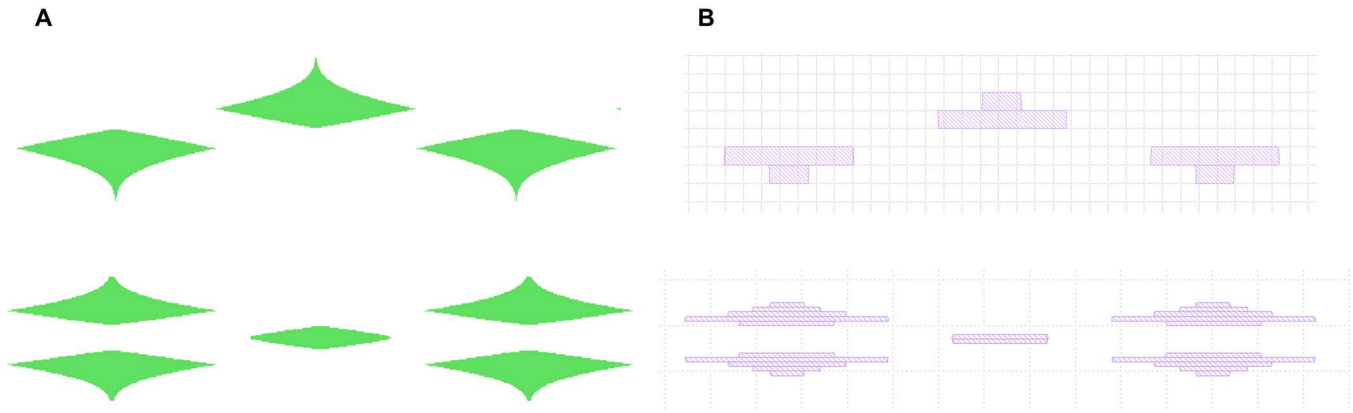

Fig. 5. Approximating the ideal NPC structure. (**A**) Ideal nonlinear hologram based on Eq. 2 (**B**) approximated shapes used for shaping the KTP crystals. The nonlinear holograms were fabricated using electric field poling on a large (40 mm by 40 mm by 1 mm) KTP wafer, with different combinations of HG_{01} and HG_{02} patterns that varied in width (in the *Y* axis). Some of the designs were shaped using a set of rectangles. This approximates the ideal modulation pattern and takes into account the high anisotropy of the crystal. The high-quality patterns were selected, cut, and polished. For the HG_{01}, the set of rectangles was successfully poled though the entire crystal poling length (3 cm). From it, a 1-cm crystal was cut and polished.

minimum error when compared to the tomographic data. The density matrix design is chosen to ensure hermiticity.

Supplementary Materials

This PDF file includes:

Supplementary Text
Fig. S1
References

REFERENCES AND NOTES

1. D. Gabor, A new microscopic principle. *Nature* **161**, 777–778 (1948).
2. B. E. Saleh, M. Teich, *Fundamentals of Photonics. Third edition. Hoboken, New Jersey, Wiley.* .
3. Y. Shechtman, S. J. Sahl, A. S. Backer, W. E. Moerner, Optimal point spread function design for 3D imaging. *Phys. Rev. Lett.* **113**, 1–5 (2014).
4. J. E. Curtis, B. A. Koss, D. G. Grier, Dynamic holographic optical tweezers. *Opt. Commun.* **207**, 169–256 (2002).
5. A. E. Willner, K. Pang, H. Song, K. Zou, H. Zhou, Orbital angular momentum of light for communications. *Appl. Phys. Rev.* **8**, 041312 (2021).
6. A. Carnicer, B. Javidi, Optical security and authentication using nanoscale and thin-film structures. *Adv. Opt. Photonics.* **9**, 218 (2017).
7. R. W. Boyd, *Nonlinear Optics* (Academic Press, 2008).
8. T. Ellenbogen, N. Voloch-Bloch, A. Ganany-Padowicz, A. Arie, Nonlinear generation and manipulation of airy beams. *Nat. Photonics.* **3**, 395–398 (2009).
9. A. Arie, N. Voloch, Periodic, quasi-periodic, and random quadratic nonlinear photonic crystals. *Laser Photonics Rev.* **4**, 355–373 (2010).
10. A. Shapira, L. Naor, A. Arie, Nonlinear optical holograms for spatial and spectral shaping of light waves. *Sci. Bull.* **60**, 1403–1415 (2015).
11. A. Shapira, I. Juwiler, A. Arie, Nonlinear computer-generated holograms. *Opt. Lett.* **36**, 3015–3017 (2011).
12. A. Shapira, R. Shiloh, I. Juwiler, A. Arie, Two-dimensional nonlinear beam shaping: erratum. *Opt. Lett.* **37**, 4795 (2012).
13. Y. Zhang, Y. Sheng, S. Zhu, M. Xiao, W. Krolikowski, Nonlinear photonic crystals: From 2D to 3D. *Optica.* **8**, 372 (2021).
14. I. Dolev, T. Ellenbogen, A. Arie, Switching the acceleration direction of Airy beams by a nonlinear optical process. *Opt. Lett.* **35**, 1581–1583 (2010).
15. N. V. Bloch, K. Shemer, A. Shapira, R. Shiloh, I. Juwiler, A. Arie, Twisting light by nonlinear photonic crystals. *Phys. Rev. Lett.* **108**, 1–5 (2012).
16. P. Chen, C. Wang, D. Wei, Y. Hu, X. Xu, J. Li, D. Wu, J. Ma, S. Ji, L. Zhang, L. Xu, T. Wang, C. Xu, J. Chu, S. Zhu, M. Xiao, Y. Zhang, Quasi-phase-matching-division multiplexing holography in a three-dimensional nonlinear photonic crystal. *Light Sci. Appl.* **10**, 146 (2021).
17. N. G. R. Broderick, G. W. Ross, H. L. Offerhaus, D. J. Richardson, D. C. Hanna, Hexagonally poled lithium niobate: A two-dimensional nonlinear photonic crystal. *Phys. Rev. Lett.* **84**, 4345–4348 (2000).
18. V. Berger, Nonlinear photonic crystals. *Phys. Rev. Lett.* **81**, 4136–4139 (1998).
19. W.-H. Lee, Binary computer-generated holograms. *Appl. Optics* **18**, 3661–3669 (1979).
20. A. W. Lohmann, D. P. Paris, Binary fraunhofer holograms, generated by computer. *Appl. Optics* **6**, 1739–1748 (1967).
21. A. Anwar, C. Perumangatt, F. Steinlechner, T. Jennewein, A. Ling, Entangled photon-pair sources based on three-wave mixing in bulk crystals. *Rev. Sci. Instrum.* **92**, 041101 (2021).
22. M. Kues, C. Reimer, J. M. Lukens, W. J. Munro, A. M. Weiner, D. J. Moss, R. Morandotti, Quantum optical microcombs. *Nat. Photonics* **13**, 170–179 (2019).
23. A. M. Brańczyk, A. Fedrizzi, T. M. Stace, T. C. Ralph, A. G. White, Engineered optical nonlinearity for quantum light sources. *Opt. Express* **19**, 55–65 (2011).
24. A. Dosseva, Ł. Cincio, A. M. Brańczyk, Shaping the joint spectrum of down-converted photons through optimized custom poling. *Phys. Rev. A* **93**, 013801 (2016).
25. A. Forbes, I. Nape, Quantum mechanics with patterns of light: Progress in high dimensional and multidimensional entanglement with structured light. *AVS Quantum Sci.* **1**, 011701 (2019).
26. M. Erhard, M. Krenn, A. Zeilinger, Advances in high-dimensional quantum entanglement. *Nat. Rev. Phys.* **2**, 365–381 (2020).
27. N. J. Cerf, M. Bourennane, A. Karlsson, N. Gisin, Security of quantum key distribution using d-level systems. *Phys. Rev. Lett.* **88**, 127902 (2002).
28. D. Bruß, C. Macchiavello, Optimal eavesdropping in cryptography with three-dimensional quantum states. *Phys. Rev. Lett.* **88**, 4 (2002).
29. A. Mair, A. Vaziri, G. Weihs, A. Zeilinger, Entanglement of the orbital angular momentum states of photons. *Nature* **412**, 313–316 (2001).
30. A. C. Dada, J. Leach, G. S. Buller, M. J. Padgett, E. Andersson, Experimental high-dimensional two-photon entanglement and violations of generalized Bell inequalities. *Nat. Phys.* **7**, 677–680 (2011).
31. E. Rozenberg, A. Karnieli, O. Yesharim, J. Foley-Comer, S. Trajtenberg-Mills, D. Freedman, A. M. Bronstein, A. Arie, Inverse design of spontaneous parametric downconversion for generation of high-dimensional qudits. *Optica* **9**, 602–615 (2022).
32. Y. Ming, J. Tang, Z. X. Chen, F. Xu, L. J. Zhang, Y. Q. Lu, Generation of N00N state with orbital angular momentum in a twisted nonlinear photonic crystal. *IEEE J. Sel. Top. Quantum Electron.* **21**, 225–230 (2015).
33. Q. Yu, C. Xu, S. Chen, P. Chen, S. Nie, S. Ke, D. Wei, M. Xiao, Y. Zhang, Manipulating orbital angular momentum entanglement in three-dimensional spiral nonlinear photonic crystals. *Photonics* **9**, 504 (2022).
34. C. Xu, S. Huang, Q. Yu, D. Wei, P. Chen, S. Nie, Y. Zhang, M. Xiao, Manipulating the orbital-angular-momentum correlation of entangled two-photon states in three-dimensional nonlinear photonic crystals. *Phys. Rev. A* **104**, 063716 (2021).
35. P. Urenski, M. Lesnykh, Y. Rosenwaks, G. Rosenman, M. Molotskii, Anisotropic domain structure of $KTiOPO_4$ crystals. *J. Appl. Phys.* **90**, 1950–1954 (2001).
36. E. V. Kovlakov, I. B. Bobrov, S. S. Straupe, S. P. Kulik, Spatial bell-state generation without transverse mode subspace postselection. *Phys. Rev. Lett.* **118**, 030503 (2017).

37. S. P. Walborn, A. H. Pimentel, Generalized Hermite-Gauss decomposition of the two-photon state produced by spontaneous parametric down conversion. *J. Phys. B At. Mol. Opt. Phys.* **45**, 165502 (2012).
38. S. Trajtenberg-Mills, I. Juwiler, A. Arie, On-axis shaping of second-harmonic beams. *Laser Photonics Rev.* **9**, L40–L44 (2015).
39. S. P. Walborn, S. Pádua, C. H. Monken, Conservation and entanglement of Hermite-Gaussian modes in parametric down-conversion. *Phys. Rev. A - At. Mol. Opt. Phys.* **71**, 053812 (2005).
40. M. Fiorentino, S. M. Spillane, R. G. Beausoleil, T. D. Roberts, P. Battle, M. W. Munro, Spontaneous parametric down-conversion in periodically poled KTP waveguides and bulk crystals. *Opt. Express* **15**, 7479–7488 (2007).
41. E. Bolduc, N. Bent, E. Santamato, E. Karimi, R. W. Boyd, Exact solution to simultaneous intensity and phase encryption with a single phase-only hologram. *Opt. Lett.* **38**, 3546–3549 (2013).
42. S. Trajtenberg-Mills, A. Karnieli, N. Voloch-Bloch, E. Megidish, H. S. Eisenberg, A. Arie, Simulating correlations of structured spontaneously down-converted photon pairs. *Laser Photonics Rev.* **14**, 1–11 (2020).
43. B. Jack, A. M. Yao, J. Leach, J. Romero, S. Franke-Arnold, D. G. Ireland, S. M. Barnett, M. J. Padgett, Entanglement of arbitrary superpositions of modes within two-dimensional orbital angular momentum state spaces. *Phys. Rev. A - At. Mol. Opt. Phys.* **81**, 043844 (2010).
44. E. Toninelli, B. Ndagano, A. Vallés, B. Sephton, I. Nape, A. Ambrosio, F. Capasso, M. J. Padgett, A. Forbes, Concepts in quantum state tomography and classical implementation with intense light: A tutorial. *Adv. Opt. Photonics* **11**, 67–134 (2019).
45. D. F. V. James, P. G. Kwiat, W. J. Munro, A. G. White, Measurement of qubits. *Phys. Rev. A - At. Mol. Opt. Phys.* **64**, 052312 (2001).
46. A. K. Ekert, Quantum cryptography and Bell's theorem, in *Quantum Measurements in Optics*, P. Tombesi, D. F., Walls, Eds. (Springer, 1992), pp. 413–418.
47. N. Gisin, G. Ribordy, W. Tittel, H. Zbinden, Quantum cryptography. *Rev. Mod. Phys.* **74**, 145–195 (2002).
48. W. Tittel, J. Brendel, H. Zbinden, N. Gisin, Violation of bell inequalities by photons more than 10 km apart. *Phys. Rev. Lett.* **81**, 3563–3566 (1998).
49. K. Buse, J. Imbrock, E. Krätzig, K. Peithmann, Photorefractive effects in LiNbO3 and LiTaO3, in *Photorefractive Materials and Their Applications 2: Materials*, P. Günter, J.-P. Huignard, Eds. (Springer New York, 2007), pp. 83–126.
50. F. Mondain, F. Brunel, X. Hua, E. Gouzien, A. Zavatta, T. Lunghi, F. Doutre, M. P. De Micheli, S. Tanzilli, V. D'Auria, Photorefractive effect in $LiNbO_3$-based integrated-optical circuits for continuous variable experiments. *Opt. Express* **28**, 23176–23188 (2020).
51. Z. Tang, R. Chandrasekara, Y. C. Tan, C. Cheng, L. Sha, G. C. Hiang, D. K. L. Oi, A. Ling, Generation and analysis of correlated pairs of photons aboard a nanosatellite. *Phys. Rev. Appl.* **5**, 054022 (2016).
52. F. Dai, Q. Tian, S. Huang, M. Wang, Y. Sheng, Y. Li, H. Wang, Photon pair generation in lithium niobate waveguide periodically poled by femtosecond laser. *Chin. Opt. Lett.* , 1–5 (2022).
53. L. T. Feng, M. Zhang, X. Xiong, Y. Chen, H. Wu, M. Li, G. P. Guo, G. C. Guo, D. X. Dai, X. F. Ren, On-chip transverse-mode entangled photon pair source. *npj Quantum Inf.* **5**, 1–7 (2019).
54. A. Mohanty, M. Zhang, A. Dutt, S. Ramelow, P. Nussenzveig, M. Lipson, Quantum interference between transverse spatial waveguide modes. *Nat. Commun.* **8**, 1–7 (2017).
55. D. Wei, C. Wang, H. Wang, X. Hu, D. Wei, X. Fang, Experimental demonstration of a three-dimensional lithium niobate nonlinear photonic crystal. *Nat. Photonics.* **12**, 596–600 (2018).
56. D. Wei, C. Wang, X. Xu, H. Wang, Y. Hu, P. Chen, J. Li, Y. Zhu, C. Xin, X. Hu, Y. Zhang, D. Wu, J. Chu, S. Zhu, M. Xiao, Efficient nonlinear beam shaping in three-dimensional lithium niobate nonlinear photonic crystals. *Nat. Commun.* **10**, 1–7 (2019).
57. A. S. Solntsev, G. S. Agarwal, Y. Y. Kivshar, Metasurfaces for quantum photonics. *Nat. Photonics.* **15**, 327–336 (2021).
58. J. Heinze, K. Danzmann, B. Willke, H. Vahlbruch, 10 dB quantum-enhanced michelson interferometer with balanced homodyne detection. *Phys. Rev. Lett.* **129**, 031101 (2022).
59. J. Schneeloch, J. C. Howell, Introduction to the transverse spatial correlations in spontaneous parametric down-conversion through the biphoton birth zone. *J. Opt.* **18**, 053501 (2016).
60. E. V. Kovlakov, S. S. Straupe, S. P. Kulik, Quantum state engineering with twisted photons via adaptive shaping of the pump beam. *Phys. Rev. A* **98**, 060301 (2018).

Acknowledgments: We thank Z. Gefen from Raicol crystals for assistance in preparing the NPCs. **Funding:** This work was funded by the Israel Science Foundation (969/22); Ministry of Science, Technology and Space; The Israel Innovation Authority; and the Tel Aviv University Center for Quantum Science and Technology. **Author contributions:** Designing the nonlinear crystals: O.Y. and I.J. Designing and building the experimental setup: O.Y. and S.P. Analyzing the experimental data: O.Y. and J.F.-C. Supervision: A.A. Writing—original draft: O.Y. Writing—review and editing: O.Y., S.P., J.F.-C., and A.A. **Competing interests:** The authors declare that they have no competing interests. **Data and materials availability:** All data needed to evaluate the conclusions in the paper are present in the paper and/or the Supplementary Materials. Coincidence count variances are available at https://doi.org/10.5061/dryad.m63xsj468.

Submitted 8 September 2022
Accepted 20 January 2023
Published 24 February 2023
10.1126/sciadv.ade7968